journal

J. Am. Ceram. Soc., 86 [3] 373–86 (2003)

Exploiting Covalency to Enhance Metal–Oxide and Oxide–Oxide Adhesion at Heterogeneous Interfaces

Emily A. A. Jarvis and Emily A. Carter

Department of Chemistry and Biochemistry, University of California, Los Angeles, Los Angeles, California 90095-1569

We employ first-principles density functional calculations to explore atomic-level interactions and predict the ideal work of adhesion at the SiO_2/nickel and ZrO_2/SiO_2 interfaces. We find that chemical bonding at the interface serves to strengthen significantly interfaces formed with SiO_2, which exhibits significant covalent bonding character, relative to those formed using more ionic oxides, such as Al_2O_3, in place of SiO_2. The improved strength of these interfaces due to local bonding interactions may hold materials design implications for practical applications that require optimal adhesion between metal-ceramic layered structures, including thermal barrier coatings.

I. Introduction

ACHIEVING well-matched heterogeneous interfaces is crucial for numerous practical applications. Although matching bulk properties for the constituents of such interfaces is fairly straightforward, these properties alone cannot ensure optimal interface design. In particular, unique features relevant to thin films, amorphous structures, and the local interatomic interactions may have a significant impact on the resulting behavior—even for macroscopically thick interfaces. Unfortunately, it is these properties that are often not well-understood and generally very difficult to characterize. This prevents detailed predictive design for heterogeneous interface applications. A wealth of empirical knowledge does exist, but conclusions and trends that can be inferred from these studies are generally very conditions-dependent.

One example where optimization of interface behavior is crucial and nontrivial is in the case of thermal barrier coatings (TBCs) for jet engine turbines. TBCs serve the valuable role of protection against thermal and corrosive degradation of the superalloy turbine blades in the harsh combustion environment.[1,2] Such applications require optimization of several coating and interface properties for maximum effectiveness. Among these, favorable adhesion, well-matched thermal expansion coefficients, effective thermal protection, and protection against hot oxidation/corrosion are especially vital properties that these coatings must possess.[3] For TBCs, matching even the bulk properties over the harsh temperature and chemical potential ranges is a challenge.

A typical structure for a TBC consists of several layers. The superalloy substrate is a single-crystal alloy of primarily Ni_3Al in a nickel matrix. Generally, a metal alloy bond coat is deposited on the superalloy substrate: two common bond coatings are MCrAlY (where M = Ni, Fe, and/or Co) and PtAl alloys.[4] A thin Y_2O_3-stabilized ZrO_2 (YSZ) film then serves as the top coat and provides the primary thermal protection for the underlying substrate. Because oxygen diffuses through ZrO_2 at high temperature and along cracks and grain boundaries at all relevant temperatures, the metal alloy bond coat must provide some means of oxidation/corrosion protection for the superalloy. This goal partially motivates the aluminum content in the bond-coat alloy, since alumina (Al_2O_3) provides a slow-growing oxide that effectively protects the underlying alloy from further oxidation. This layer is known as the thermally grown oxide (TGO).

The TGO layer is a site where TBC failure mechanisms are particularly concentrated. With repeated thermal cycling, the thermal barrier coating spalls. This failure can occur at the ZrO_2/Al_2O_3 interface but is especially prone within the Al_2O_3 TGO layer and at the interface of the metal alloy bond coat with Al_2O_3.[5] Addition of reactive elements can improve oxidation resistance, but the role of these remains incompletely understood.[6–9]

Although alumina is the preferred TGO in most current applications, other oxides may also serve in this role. Generally, a successful protective oxide must exhibit slow growth in order to (i) limit strains resulting from thermal expansion mismatch between the oxide scale and the metal alloy and (ii) avoid depletion of the oxidation element from this alloy. Chromia, alumina, and silica all exhibit potential uses in this capacity.[10] In fact, it has been speculated that silica coatings should provide a more ideal diffusion barrier, because these generally form amorphous layers that do not allow diffusion along grain boundaries, etc.[11] Likewise, silica should provide the slowest-growing oxide,[12] which may be useful for limiting strain and/or dopant depletion failure of the

R. H. French—contributing editor

Manuscript No. 186921. Received June 18, 2002; approved October 9, 2002.

This work was supported by the U.S. Air Force Office of Scientific Research, which provided funding and computing resources. Computing time was provided through a U.S. Air Force-sponsored Challenge Grant at the Maui High Performance Computing Center.

Based in part on the dissertation submitted by author EAAJ for the Ph.D. degree in chemistry at the University of California, Los Angeles, CA, 2002.

Feature

bond coat alloy. Here, we use first-principles methods to investigate the potential for SiO_2 to substitute successfully for Al_2O_3 as the TGO.

For years it has been known that silicon might dramatically improve oxidation resistance of certain metal alloys (by the formation of an α-SiO_2 scale);[13] however, its use has been limited, since Si content tends to have detrimental effects on the mechanical properties of iron, nickel, and cobalt alloys.[7] Nevertheless, it is possible that very low concentrations of silicon—i.e., 0.9% in the case of a steel with 20% chromium and 25% nickel—could provide maximum benefit[14] and form an underlying SiO_2 protective layer,[15] while still allowing good mechanical properties of the alloy. Sulfur segregation to alloy/scale interfaces has been linked with spallation at these interfaces.[16] Silica coatings on stainless steels (Incoloy 800H, which consists of ~46% iron, ~21% chromium, and ~31% nickel,[17] as well as AISI 304, 310, and 321[18]) have also been shown to provide effective sulfur protection, which may be crucial in TBC applications. The SiO_2 phase in these coatings was not certain but was speculated to be α-SiO_2.[18] In a recent test of ceramics designed to replace chromia for stainless-steel protective coatings, silica was determined to be the most effective pure ceramic that was studied; it was better than either titania or zirconia in providing corrosion resistance.[19]

Silicon has been added to nickel alloys with favorable effects on both oxidation resistance and adhesion. An experimental study showed the parabolic rate constant of the oxide growth kinetics decreased for oxidation of the nickel superalloy at 900°C; the study also showed that the oxide adhesion increased for scales formed during 1100°C oxidation.[20] Although amorphous silica-coated Ni-20Cr has been shown to protect the nickel from oxidation and reduce the oxidation rate, this rate reduction is not necessarily attributed to protection provided by silica. Another possible explanation is that silica may act as a reactive element to modify the growth of Cr_2O_3 on this alloy, so that the protective chromia layer forms more rapidly and the subsequent growth mechanism of that oxide is altered.[21] Recent scanning transmission electron microscopy (STEM) investigations of the oxidation of a Ni-20Cr alloy showed that a thin protective silica layer forms at earlier oxidation times than had been anticipated previously. Likewise, this amorphous layer adheres to the alloy, despite the fact that the Ni-20Cr alloy contained sulfur and no reactive elements to getter this sulfur content. The authors did not observe sulfur segregation to the metal/oxide interface.[22]

Investigation of the crystallization and phase stability of several nickel–silicon alloys, using ion-beam analysis, transmission electron microscopy (TEM), and X-ray diffractometry (XRD), has shown the formation of an epitaxial relation between Ni_3Si and nickel; this relation is attributed to highly favorable lattice matching.[23] XRD studies of $NiSi_2$ grain growth on SiO_2 (formed by thermally oxidizing single-crystal Si(100)) have shown that these grains grow preferentially with the (111) planes parallel to the substrate, which was believed to reduce both interfacial and surface energies, and TEM showed the $NiSi_2$ phase to be stable up to 800°C in these grains.[24] A study of the oxidation of ~Ni_3Si and nickel–silicon–chromium alloys suggested that the initial formation of nonprotective oxides is followed by protective, amorphous silica scale formation at 700°C.[25] For temperatures of <800°C, the chromium content seems to be beneficial in limiting the oxidation rates; at higher temperatures, this trend is reversed—chromium content increased the oxidation rates. These results led the authors to suggest that amorphous silica provides a more protective scale at high temperatures.[25] In addition to oxidation resistance, it is also possible that silicon additions to nickel alloys can improve the thermal expansion coefficients of these alloys for nickel superalloy coating applications.[26] Accordingly, although many details remain to be optimized, these recent studies provide some insight into the behavior of silicon content in nickel alloys.

(1) Aspects of Metal/Ceramic and Ceramic/Ceramic Adhesion

An absolute value of adhesion at heterogeneous interfaces is difficult to isolate via experimental means. One reason for this is the difficulty in distinguishing processes arising from different phenomena and length scales. Phase changes, chemical reactivity, and segregation of impurities also affect the measurements in realistic systems. Accordingly, measured adhesion values often comprise a variety of features, which complicates the predictive optimization of the interfaces of materials.

Traditionally, experimental measures of ceramic–metal adhesion focus on solid/liquid interfaces. This approach may provide a good estimate to solid/solid interface energetics, but it is not always the case; the assumption that the adhesion between materials is relatively constant—regardless of phase—is often unsatisfactory. A particular example where such an approximation fails is in the case of SiO_2/Ni, where atomic force microscopy (AFM) has shown amorphous nickel particles weakly adhere to a substrate of amorphous, submicrospheres of silica, but polycrystalline nickel particles strongly adhere to the same substrate material.[27]

(2) Silica/Nickel Interface

Nickel films grown on a silica substrate have been shown to prefer the (111) orientation; this preference becomes more pronounced as the temperature increases.[28] A detailed characterization of the interface is not available. As mentioned, AFM studies have shown that polycrystalline nickel particles adhere to silica substrates much more strongly than their amorphous counterparts. This observed difference in adhesion between amorphous and polycrystalline nickel on amorphous silica led Ramesh *et al.*[27] to speculate that a silicate phase was formed at the interface of polycrystalline SiO_2/Ni, with perhaps $Si–O^{\delta-}–Ni^{\delta+}$ bonding, as indicated by infrared (IR) spectroscopy.[29] It is not obvious why polycrystalline nickel would be more reactive than amorphous nickel toward SiO_2; indeed, one might have expected the opposite.

An early study by Sangiorgi *et al.*[30] suggested that chemical bonding of both metal–oxygen and metal–silicon varieties was required to explain the adhesion for certain nonreactive liquid metals (gold and lead) on (quartz and vitreous) silica substrates. This conclusion relied on correlations with the work of adhesion measurements. Later work that was fit instead to work of immersion suggested that the dominant interactions for interfaces between metals and ceramics with significant ionic character are instead related to van der Waals and image charge contributions.[31] Density functional theory (DFT) cluster calculations of Cu atoms and clusters on a SiO_2 surface (derived from α-quartz) suggest that polarization is the primary attractive mechanism for the perfect SiO_2 surface, but that defect sites allow strong bonds to form between the metal and the ceramic.[32] DFT calculations on the interactions of nickel that is deposited on SiC substrates show Ni–Si bonding,[33] but the SiC crystal exhibits much more covalent bonding than SiO_2. Accordingly, comparisons of Ni–Si electronic properties of SiC versus SiO_2 substrates cannot be inferred directly. To our knowledge, no DFT simulations of the SiO_2/nickel interface have been reported before our work.

Most studies of metal/SiO_2 interfaces have investigated metal deposition on amorphous or quartz silica substrates. Crystalline silica thin-film growth on metal substrates has been achieved only recently for SiO_2/molybdenum interfaces.[34] Generally, silica growth on metal substrates results in amorphous silica, even if a stoichiometric film is created. Studies employing scanning electron microscopy (SEM), energy-dispersive spectroscopy (EDS), and XRD to investigate the interface of liquid nickel superalloys that are in contact with a silica substrate (with 25% porosity) at high temperature (1390°C) find that interfaces between oxides of the reactive elements and silica form at these high temperatures, rather than a metal/silica interface,[35] due to the inclusion of dopants with high oxygen affinity in the alloy.

(3) Zirconia/Silica Interface

The ceramic–ceramic ZrO_2/SiO_2 interface is receiving increased attention, because of its potential use as a gate dielectric in electronic devices. Medium-energy ion-scattering studies (MEIS) have shown that ZrO_2 can form sharp interfaces with silica at temperatures up to 900°C (at which point silicates were formed under the conditions present in that study).[36] SEM and TEM

studies have also shown good bonding with effective wetting between a ZrO_2 film and glass ceramics.[37] Although silica has a very low solubility in YSZ, amorphous SiO_2 will readily form along grain boundaries of this material.[38] Zirconium is effective at reducing oxides of silicon; however, a stoichiometric ZrO_2 film on a silicon substrate permits silicon oxidation, especially above ~400°–500°C.[39,40] This is to be expected, because ZrO_2 does not provide adequate elevated-temperature oxidation protection, as also observed in TBC applications. Although SiO_2 growth can be problematic for electronics applications, a thin layer of this protective oxide might serve as a desirable TGO in TBCs. Binary oxides of SiO_2 and ZrO_2 can permit stabilization of the tetragonal phase of ZrO_2 by what were speculated to be covalent Si–O–Zr bonds.[41] Tetragonal ZrO_2 stabilization has also been observed in zirconia–alumina nanolaminates.[42] Since this tetragonal ZrO_2 phase is the one desired in TBC applications, this also might prove to be a useful property of SiO_2–ZrO_2 interactions. Although generally YSZ is fairly robust against high-temperature degradation, it is prone to aging in air at moderate temperature (~150°–400°C); silica (cristobalite phase at the *t*-ZrO_2 polycrystal surface) and $ZrSiO_4$ can inhibit this undesirable phenomenon.[43]

To our knowledge, first-principles DFT calculations of the ZrO_2/SiO_2 interface have not been performed elsewhere. Recent DFT calculations that predict the stability of bulk ZrO_2 in contact with bulk SiO_2 and silicon indicate that both interfaces should be (slightly) thermodynamically unstable, with the reaction of ZrO_2 and SiO_2 combining to form $ZrSiO_4$, displaying a small negative enthalpy.[44] Naturally, kinetic effects limit this reaction in practice.

Only a limited understanding of SiO_2 substrates with stabilized ZrO_2 coatings for potential TBC applications is available. The thermal conductivity of YSZ has been shown to be independent of substrate when comparing polycrystalline alumina, Al_2O_3(0001), the (111) and (100) faces of ZrO_2, and fused quartz substrates.[45] Coatings of Al_2O_3-stabilized ZrO_2 have been deposited on silica substrates, and XRD has shown that the cubic phase of ZrO_2 (*c*-ZrO_2) forms at 600°C from an initially amorphous film under such conditions.[46] The potential of mullite (Al_2O_3 and SiO_2) and/or mullite with YSZ protective coatings has been investigated for protection of SiC and Si_3N_4 for use in combustion environments; the ZrO_2 top coat seems to be effective in eliminating some of the unfavorable features (e.g., silica volatilization) of a SiO_2-based protective coating.[47] More study is needed to understand the behavior of similar multilayer coatings on metal alloy substrates; the present work is a step in this direction, where we explore the interactions at both ZrO_2/SiO_2 and SiO_2/Ni interfaces.

II. Theoretical Methods

We performed spin-polarized density functional calculations[48] within the Vienna Ab Initio Simulation Package (VASP).[49] In these calculations, the valence electron density is expanded in a plane-wave basis and ultrasoft pseudopotentials[50] replace the core electrons and nucleus. Periodic boundary conditions allow "infinite" bulk crystals to be simulated, even though the number of unique atomic positions is limited to <150 atoms in the calculations reported here. The exchange-correlation potential is approximated by the generalized gradient functional of Perdew and Wang, circa 1991 (GGA-PW91).[51]

The pseudopotentials used here have been described elsewhere,[52–54] with the exception of the one for silicon, for which we used the standard silicon ultrasoft pseudopotential in the VASP version 4.4 database. We used two different zirconium pseudopotentials: one affords explicit treatment of the valence 5*s* and 4*d* electrons, and the other provides explicit treatment of the 4*p* electrons as well. The specific results in the discussion of the ZrO_2/SiO_2 interface refer to this latter pseudopotential. Nonlinear partial core corrections to the exchange-correlation potential are included for all elements except oxygen.[55]

Kinetic-energy cutoffs of ~340 eV for the pseudodensity and 554 eV for the augmentation density are used. The Brillouin zone is sampled with a Monkhorst–Pack grid[56] of $1 \times 5 \times 5$ for the SiO_2/Ni interfaces and $1 \times 3 \times 3$ for the ZrO_2/SiO_2 interfaces, resulting in thirteen and five irreducible *k*-points, respectively. In each case, these choices of bases and *k*-point sampling converged the total energy (extrapolated from the free energy[57]) to the meV/atom range. Two different methods for setting the partial occupancies near the Fermi level are used to enhance convergence: first-order Methfessel–Paxton smearing,[58] and the tetrahedron method with corrections introduced by Blöchl *et al.*[59] The smearing method was used in the density of states (DOS) plots that are presented later, because of the small number of irreducible *k*-points that are used in the large calculation supercells.

The atomic relaxations are performed using a conjugate gradient algorithm. To test whether or not our structures were converged to a favorable minimum energy atomic configuration, we performed limited high-temperature (at 1200 and 1400 K) annealing runs, using timesteps of ~0.35 fs for up to ~0.4 ps trajectories.[60] Although we found no new features after annealing/quenching, it is possible that, with longer annealing runs and/or higher-temperature annealing, new reaction products could form;[†] this is left to future work. In the atomic relaxations and molecular dynamics (MD) simulations, the positions of all atoms within the ceramic film and the top two layers of the three-monolayer (ML)-thick Ni(111) substrate are free to relax. In the ZrO_2/SiO_2 calculations, we chose a SiO_2 substrate thickness of six ML, with the bottom three ML fixed to bulk values. These frozen substrate coordinates away from the interface were employed to better simulate a macroscopically thick substrate. Generally, the inclusion of ~10 Å of vacuum in the periodic surface and interface cells was adequate for converged total energies. Occasionally, a small artificial dipolar interaction between slab images that had non-negligible impact on the total energy (i.e., ~0.1 eV) was found in the direction perpendicular to the interface, which was effectively reduced by the inclusion of ~15 Å of vacuum. The relaxed atomic coordinates were not sensitive to these minor changes.

We define projection spheres around each atomic site for the purposes of analyzing the local *s*, *p*, and *d* occupation, DOS, etc. These projection radii have no impact on the charge density or energy convergence in the calculation; rather, they are simply used for post-calculation analysis purposes. The choice of the integration sphere is not unique, as we have discussed previously.[61] Nevertheless, information provided by these local charge analyses can provide insight into trends and general features. For the metal-ceramic studies, we defined spheres with radii of 1.015 and 1.345 Å for Al and O in alumina, respectively; 1.08 and 1.26 Å for Si and O in silica, respectively; and 1.23 Å (and an alternative larger radius of 1.37 Å) for Ni. In the ZrO_2/SiO_2 studies, we use a radius of 1.4 Å for Zr, 1.08 Å for Si, and 1.3 Å for O in both the SiO_2 and ZrO_2 ceramics.

The equilibrium volumes of the bulk crystals are calculated by performing a series of single-point energy calculations, while maintaining crystalline structures with perfect symmetry but uniformly expanding or contracting the lattice vectors. The resulting energy-volume relations are fit using the equation of state described by Murnhagan,[62] as well as second- and third-order polynomials. Our methods of calculating surface and interfacial energies have been described previously.[52,53] In the interface calculations, the ideal Ni lattice vectors are imposed for the SiO_2/Ni interface and the ideal SiO_2 lattice vectors are imposed for the ZrO_2/SiO_2 interface supercell. In both cases, the resulting misfit is <2%.

III. Results and Discussion

(1) Bulk and Surface Properties

We chose to model the α-quartz phase of SiO_2 in our interface studies. The periodic boundary conditions imposed by our calculation necessitate a crystalline rather than amorphous silica phase,

[†]For instance, an olivine silicate layer of Ni_2SiO_4 forms at the SiO_2/Ni interface created by the hot pressing of powders at 1400°C. (See R. Drira-Halouani, L. Durand, and B. Lavelle, *Mater. Sci. Eng. A*, **252**, 144–48 (1998).)

and the basal plane of α-quartz is the best-characterized face of crystalline SiO_2. In addition, the studies of metal adhesion on single-crystal SiO_2 have used the quartz phase,[30] and experiments have suggested that a thin layer of silica, in perhaps an α-SiO_2 phase, might form a protective layer under certain conditions.[13,18] In future studies, alternative phases and faces of SiO_2 might provide additional insight. In our calculations, the equilibrium volumes of the α-quartz[63] and face-centered cubic (fcc) nickel agree with the experimental values to within 1%. Within the GGA, the *c*-ZrO_2 bulk volume is overestimated by $<2\%$ with the inclusion of only *s* and *d* states on the Zr and by $\sim 3.5\%$ with the inclusion of semicore *p* states on the Zr. As often found, the GGA overcorrects the well-known overbinding tendency of the local density approximation (LDA); hence, the equilibrium lattice vectors are slightly expanded. More detailed descriptions of the calculated bulk properties of ZrO_2, Al_2O_3, and nickel have been described previously.[52,53]

Low-pressure silica polymorphs exhibit a fairly open crystal structure. The largely covalent character of the Si–O bond allows highly directional bonding to be favored over close packing. The equilibrium volume of α-quartz (22.71 cm^3/mol) lies toward the high-volume end of the silica polymorphs—between the more tightly packed, high-pressure phases such as stishovite (molar volume of 14.04 cm^3) and the low-pressure stable crystal structures, such as cristobalite (molar volume of 25.76 cm^3) and glass (molar volume of 27.25 cm^3).[64] Hence, the α-quartz crystal structure exhibits fairly high initial compressibility.

The calculated bulk modulus is quite dependent on the extent of the potential energy surface that is sampled. Even more important than the fact that the SiO_2 structure is not "space-filling," the initial compressibility of SiO_2 is not primarily related to a uniform decrease in bond lengths while maintaining the perfect crystal structure, as is often assumed in calculated bulk modulus estimates. Instead, distortion of the silica tetrahedra, where bond angles change but bond lengths do not, and especially contributions from rotations of the silica tetrahedra[65] primarily account for the ease of initial compressibility and the resulting low observed bulk modulus. We find that a calculated value near the observed estimates of 38.7($\pm$ 1.0) GPa,[64] can be attained only by allowing internal relaxations and restricting sampling to very near the equilibrium volume. Excluding such distortions results in an almost fourfold overestimate of the bulk modulus (148.1 GPa versus 38.7 GPa) when sampling the region within 5%–7% of the equilibrium volume.

The surfaces of Ni(111) and ZrO_2(111) have been described previously.[52,53,66] Although SiO_2 is a material of great technological importance, the perfect crystalline surfaces often are not the surfaces of interest; instead, polycrystalline and amorphous surfaces tend to dominate practical applications. Nevertheless, the basal (0001) plane of α-quartz is perhaps the best-characterized crystalline SiO_2 surface. It is likely that this clean surface will undergo several reconstructions. These reconstructions are excluded if the periodic boundary conditions do not permit a unique surface area that is large enough to accommodate such effects. We did not perform a detailed study of surface reconstructions. However, we did start with a surface, i.e., cleavage between the two oxygen layers, that would permit similar long-range reconstructions to those that have been modeled using empirical potentials,[73] and that also allows us to model stoichiometric, nonpolar surface slabs.

Experimental reflection electron energy loss spectroscopy (REELS) studies of the SiO_2(0001) surface indicate two primary defects: oxygen vacancies and a "tridimensional disorder," which refers to an amorphization defect in the crystal structure.[67] Low-energy electron diffraction (LEED) studies have also shown that a reconstruction occurs at a temperature of $\sim$600°C, whereby the reconstruction periodic area is 84 times larger than the original surface.[68] Current direct *ab initio* methods cannot model such large length scales. However, work is under way to couple length scales[69] and develop efficient and accurate linear-scaling electronic structure theories.[70,71] Such methods eventually should allow more complete studies of these SiO_2 surface reconstructions, as well as small-percentage component contaminants, etc.

We found that the surface energy of the relaxed, unreconstructed (0001) surface of α-quartz was very well converged by a thickness of six stoichiometric SiO_2 units, $\sim$10 Å. Even a much thinner slab of only three stoichiometric SiO_2 units provided a surface energy within 1% of the converged value. The calculated surface energy of 2.30 J/m^2 is likely to be a significant overestimate, because the in-plane boundary conditions are those of the bulk hexagonal cell and exclude long-ranged reconstructions that would otherwise serve to reduce the surface energy. A previous estimate of the (0001) surface energy of α-quartz, using a self-consistent tight-binding method, is nearly twice as large, at 4.49 J/m^2.[72] The accuracy of this estimate suffers both from similar exclusion of long-ranged reconstructions and limited self-consistency (and other approximations) in the electronic structure calculation. A recent study used *ab initio* and empirical methods to study the basal plane of α-quartz, but they did not report energetics. They found that formation of three- and six-membered ring surface reconstruction structures represented local minima using the same initial cleavage conditions as those used here.[73]

(2) SiO_2(0001)/Ni(111) Interface

Matching the surfaces of Ni(111) with SiO_2(0001) requires only a 1.3% imposed misfit for a unique interface area of 21.44 $Å^2$. This misfit results in very minor unphysical strain imposed by the periodic boundary conditions. Since we are modeling the thickening of SiO_2 on a nickel substrate, we chose to impose the bulk lattice vectors of the metal. This means that the SiO_2 films initially were formed using the perfect α-quartz atomic coordinates expanded in the interface plane by 1.3% to present a commensurate lattice to that of the substrate. Over the course of the simulation, these coordinates were permitted to relax to a more energetically favorable configuration; however, little change in the SiO_2 structure is observed on relaxation, further confirming the minimal imposed lattice strain.

We studied the effect of increasing thickness of the stoichiometric silica film on the SiO_2/Ni interface. For all thicknesses, the relaxed SiO_2 films maintain a structure very similar to the initial (bulklike) coordinates. Minor relaxations serve to stabilize the interface, i.e., the interfacial oxygen relaxes to a more favorable Ni–O–Ni interaction; however, no phase changes or dramatic rearrangements are observed. We find similar interactions for silica coatings three, six, and nine ML thick on a Ni(111) substrate. The adhesion energy is similar in the three cases, with a calculated adhesion of 1.29 J/m^2 for the 3-ML coating, 1.37 J/m^2 for the 6-ML coating, and 1.37 J/m^2 for the 9-ML coating. These differences correspond to at most a 0.1 eV difference, for the three different silica film thicknesses studied, in the interface total energy subtracted from the sum of the isolated slab (coating and substrate) energies. Effectively, the calculated adhesion remains constant for these silica films ranging from 5 to 15 Å thick. Accordingly, this estimate for the ideal work of adhesion should also apply to films of macroscopic thickness, since the 6- and 9-ML silica films exhibit regular, bulklike behavior within the center region of the film. Likewise, plastic energy dissipation mechanisms are not likely to contribute significantly for a silica coating, further supporting the relevance of the simulated interface to the macroscopic SiO_2/Ni interface. The periodic cell corresponding to the 6-ML silica coating on Ni(111) is shown in Fig. 1. F1

In addition to similar calculated adhesion values, the local atomic and electronic structure at the interface is fairly similar for the silica films that are $\geq$5 Å thick. Table I displays the Ni–O and Ni–Si bond lengths formed across the interface, as well as the Si–O bond lengths of the interfacial Si. This table also displays the site-projected charge difference for the atoms involved in interfacial bonding, at the interface relative to the charge projected onto those atoms in an isolated surface with the same atomic coordinates as the interface (i.e., where the other side of the interface has been "instantaneously" removed). In all cases, these atomic sites experience a relative reduction in the interface environment, with T1

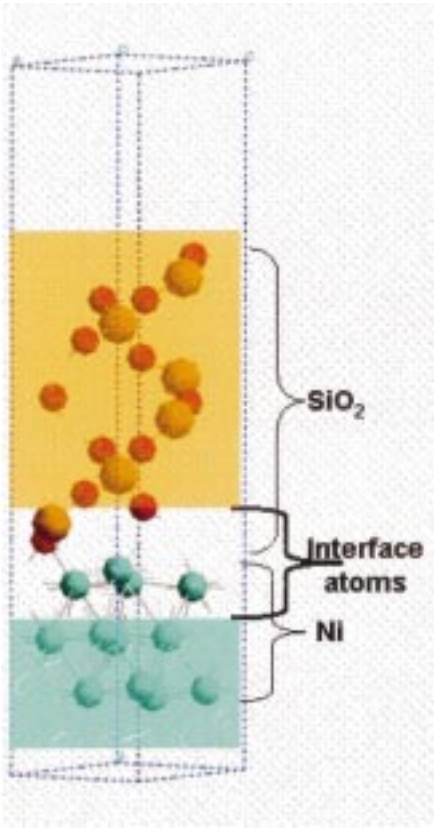

Fig. 1. Periodic cell of the 6-ML SiO_2(0001) coating on Ni(111). Si atoms are represented by light-orange, larger spheres, O atoms are indicated by dark-orange, smaller spheres, and Ni atoms are shown as light-blue stick-spheres. Substrate and coating slabs away from the interface are shaded, and the periodically unique atomic coordinates at the interface are indicated as "Interface atoms."

oxygen showing the most dramatic change (an increase of ~0.25 e in electronic charge).

For reference, the bond lengths in NiO are 2.09 Å, Ni–Si bonds in the $L1_2$ Ni_3Si structure are ~2.48 Å,[25] and the Si–O bonds in α-quartz are 1.61 Å. Hence, the Ni–Si and Ni–O bond lengths at the interface are significantly shorter than those in the respective bulk crystals, by 0.1 Å in the case of Ni–O and by >0.2 Å for Si–Ni. Concurrently, the last row in Table I shows that the Si–O bonds at the interface are weakened (stretched) to accommodate the Ni–Si and Ni–O (Si–O–Ni) bonding interactions. This straining of intraceramic bonding to maximize interfacial bonding is indicative of strong, favorable local bonding interactions at this interface.

The site-projected charge differences between the surface and interface environments all display significant increases in electronic charge at the interface. This too is indicative of chemical bonding effects at this interface. Because all atomic sites experience some electron gain, it is unlikely that ionic effects are dramatic. Instead, this charge increase on each atomic site is indicative of the formation of localized covalent-type bonds. Such bond formation is also consistent with the "straining" of intraceramic bonding, mentioned above, to permit close covalent bonding across the interface.

Although it might have been expected, we find no direct correlation between interface adhesion and the isolated surface energies of the ceramic. If a simple relationship were to hold, the ceramics with higher surface energy should adhere more strongly than those with lower energy, since the surface energy of the ceramic is a positive contribution to W_{ad}, according to the Dupré equation.[74] It is interesting to compare our predicted most stable surface energies of several ceramics with the subsequent calculated metal–ceramic adhesion energies for interfaces formed by joining those surfaces with the Ni(111) surface. The 3-ML α-SiO_2(0001) slab, as mentioned earlier, is effectively converged with respect to surface energy, and results in a surface energy of 2.3 J/m^2. For α-Al_2O_3, we predict a surface energy of 1.4 J/m^2 for the 3-ML film and a converged (0001) basal plane surface energy of 1.5 J/m^2.[53] The most stable ZrO_2 surface energy for both tetragonal and monoclinic zirconia (*t*-ZrO_2 and *m*-ZrO_2, respectively) was estimated to be ~1.2 J/m^2.[66] (For comparison, our GGA estimate of the Ni(111) surface energy is 1.9 J/m^2.[53]) The calculated ceramic/nickel adhesion is 1.4 J/m^2 for SiO_2, ~0.5 J/m^2 for Al_2O_3, and <1.0 J/m^2 for ZrO_2. If it followed that higher surface energy structures result in greater interface adhesion, the Al_2O_3 film should have adhered more strongly than the ZrO_2; instead, our calculated adhesion values for these two ceramics exhibit the reverse ordering. There is not a straightforward relation between surface energies; specific energetics of the interface—in particular, interface stabilization via local bonding interactions—are crucial to consider when explaining calculated adhesion trends.

Table II gives some sense of comparison between the local bonding interactions at the interfaces of nickel with three MLs of Al_2O_3,[53] ZrO_2,[52] and SiO_2, respectively. Similar to Table I, we

Table I. Structural and Electronic Properties of the SiO_2/Ni Interface for Three, Six, and Nine Monolayers of SiO_2[†]

Coating thickness	Ni–O bond length (Å)	Ni (e)	O (e)	Ni–Si bond length (Å)	Ni (e)	Si (e)	Si–O bond length (Å)
3 ML	2.00, 2.06	0.038, 0.033	0.230	2.25	0.142	0.087	1.62, 1.64, 1.66
6 ML	1.99, 2.06	0.025, 0.027	0.247	2.25	0.143	0.085	1.61, 1.62, 1.66
9 ML	1.98, 2.06	0.033, 0.029	0.259	2.25	0.146	0.084	1.61, 1.62, 1.66

[†]Interfacial bond lengths (Å) and the maximum site-projected charge differences (e), between the atoms involved in bonding in the interface environment and the corresponding atoms at an isolated surface, are indicated. Positive values indicate an increase in electronic charge at the interface.

Table II. Comparison of the (Shortest) Interfacial Bond Lengths and the Maximum Site-Projected Charge Differences (between the Atoms Involved in Bonding in the Interface Environment and at an Isolated Surface) at the Interface of Ni(111) with Three ML of the Oxide Ceramics[†]

Oxide	Ni–O bond length (Å)	Ni (e)	O (e)	Ni–X bond length[‡] (Å)	Ni (e)	X[‡]
Al_2O_3	2.37	0.00 (0.02)	0.03	2.32	0.13 (0.20)	0.04
ZrO_2	2.02	(0.15)	0.17	2.88	(0.18)	0.05
SiO_2	2.00	0.04 (0.09)	0.23	2.25	0.14 (0.24)	0.09

[†]No atomic site exhibits charge loss in the interface environment. Projection radii for ZrO_2 are described elsewhere.[52] Charge on Ni shows the values obtained using 1.23 Å (1.37 Å) projection radii. [‡]X is Al, Zr, or Si.

report the bond lengths and the corresponding charge projected onto each of the two atomic sites in the bond relative to the projected charge on those atoms immediately on interface cleavage. One important feature in this table is the weak Ni–O interactions of the Al_2O_3/Ni interface; i.e., the Ni–O "bond" is much longer than that formed with the other two oxides, and neither the O nor the Ni experience a dramatic change in projected charge relative to the isolated surface environment. Conversely, the Si and O in the SiO_2/Ni interface experience the greatest charge increases, relative to the cations and oxygens of the other oxides, and also form the shortest bonds with Ni. Specific choices of integration radii do affect the reported "charge gain"; nevertheless, the more favorable Ni–Si and Ni–O interactions in silica (short bonds and "shared" charge gain) and the unfavorable Ni–O interactions in alumina are consistent with the calculated adhesion trends.

At first glance, it might seem incorrect for all atomic sites to experience a "reduction" in the interface environment, such as is indicated in Tables I and II. In fact, this is not contradictory. As mentioned earlier, the projection radii for the atomic sites are not designed to be space filling—this would result in entirely unphysical results for open crystal structures and especially for surface and interface supercells that contain a vacuum region. Rather, the projection spheres indicate a region around each atomic site where the electron density reasonably can be associated with that particular site. This means that there is electron density unaccounted for in the interstitial regions; likewise, there is some flexibility in a "reasonable" choice of integration spheres. Of course, ionic and covalent bonding effects contribute to the charge difference. The general charge increase in the interface environment is primarily related to more localized electron density in the interface environment, in contrast to the surface exponential decay that is exhibited by insulating ceramics and the power-law decay of the electron density away from the surfaces of conducting metals.[75]

F2 Figure 2 displays a cross section of the electron density difference between the interface and the sum of the densities of the isolated surfaces (with the same atomic structure as the interface, i.e., where the other side of the interface has been "instantaneously" removed) for the 9-ML silica coating on the Ni(111) substrate. The lighter regions correspond to a decrease in electron density, and the darker regions represent an increase in electron density in the interface environment, with each contour corresponding to 6.7×10^{-2} e/Å^3. The total charge-density difference is conserved, i.e., equal to zero, within $<1 \times 10^{-6}$ e/Å^3. Although Figs. 2(a) and (b) may appear to experience only charge gain, recall that these panels only display a specific perpendicular two-dimensional cut near an interfacial bonding region. For regions that do not intersect bonds formed across the interface, there is a slight decrease in the delocalized density spilling into the vacuum region relative to the two surfaces. The gray background represents effectively no change (within $\sim 1 \times 10^{-3}$ e/Å^3). Relevant nuclear positions are indicated by arrows, with these positions periodically repeating along the interface. Generally, the density perturbations appear fairly minor and highly localized to the interface region. Figure 2(a) displays a cut near interfacial Ni–O bonding. Significant gain in the charge density on the O site is not apparent, which allows us to exclude dramatic NiO ionic bonding, although Table I shows an increase in electronic charge of 0.25 e on the O site. This increase is partially due to overlap with the Ni, because of the short (1.98 Å) bond that is formed between the Ni and O at the interface. Such a short bond suggests that strong Ni–O closed-shell repulsions are not present, as is also suggested by what appear to be minor charge density perturbations at the interface. Figure 2(b) displays a similar cut near an interfacial Ni–Si bond. A local Ni–Si bonding region, i.e., density buildup between the Ni–Si nuclei, is apparent in Fig. 2(b). The features in both plots suggest that covalent bonding, rather than charge transfer, may account for the site-projected charge increases on all atoms in the interface environment and the dramatic energetic stabilization that results from interface formation.

The density difference plots indicate some interfacial bonding but are not satisfactory for gaining a complete picture of the local

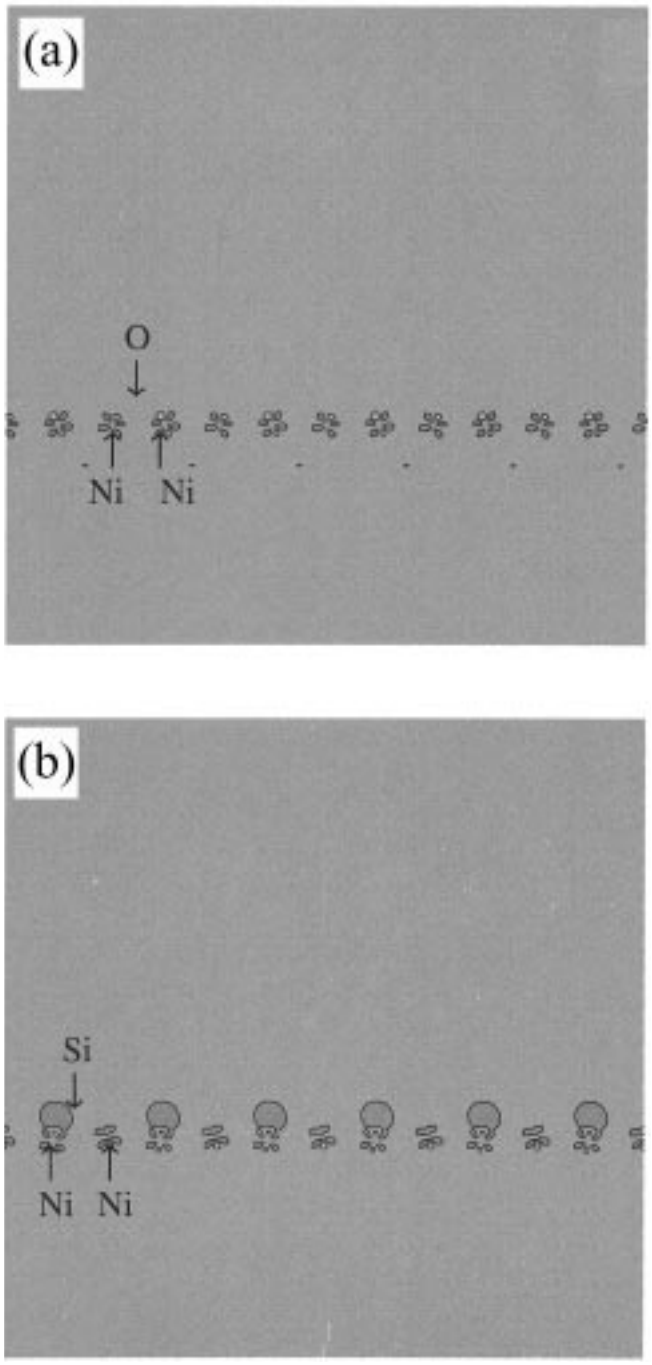

Fig. 2. Cross-sectional slice of the charge density difference between the SiO_2/Ni interface and the sum of the isolated SiO_2 and Ni slabs (a) near the Ni–O bonding region and (b) near the Ni–Si interfacial bond. Locations of the relevant nuclei are indicated by arrows. Same gray scale is used in all plots. Light regions indicate charge density loss; dark regions correspond to charge density gain at the interface relative to the sum of the isolated surfaces.

interactions that impact adhesion at this interface. Investigation of the projected local DOS provides complementary insight into the resulting electronic structural changes with interface formation. Figure 3 compares the projected local DOS on the atomic sites F3 involved in Ni–Si and Ni–O interface bonding for the interface (corresponding to the atomic sites in Table I) and the "instantaneously" cleaved surfaces. The Fermi level has been set to 0.0, with fully occupied states below this level and empty states above this level at 0 K. The unoccupied states near 1.5 eV on the O and Si in the isolated surface are one of the more dramatic features of

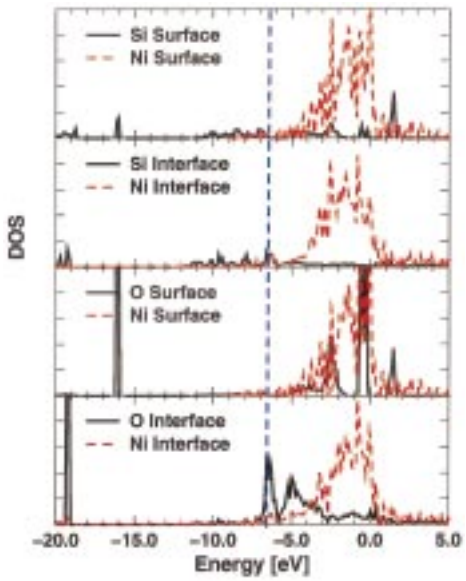

Fig. 3. Site-projected local DOS for atoms at the SiO_2/Ni interface ("Si, O, Ni Interface") and the corresponding atoms at the Ni and SiO_2 surfaces immediately upon cleavage ("Si, O, Ni Surface"). The location of occupied states that are created upon formation of the interface are indicated by the dashed line near −6.5 eV.

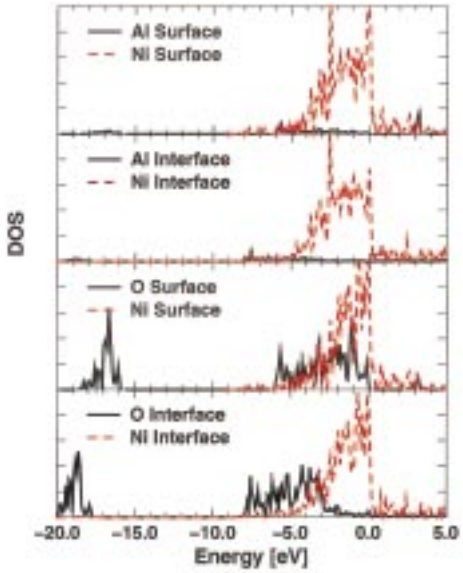

Fig. 4. Site-projected local DOS for atoms at the Al_2O_3/Ni interface ("Al, O, Ni Interface") and the corresponding atoms at the Ni and Al_2O_3 surfaces immediately upon cleavage ("Al, O, Ni Surface"). The Ni states experience little change, while the Al and O states are shifted to lower energy upon interface formation.

the surface states; these features disappear in the interface environment. This region does not correspond to typical surface gap states of the SiO_2(0001) surface; instead, these are features unique to the unrelaxed atomic coordinates of the cleaved SiO_2 film. Likewise, the lone-pair states near 0.0 eV of the surface O are a strong feature of the third panel in Fig. 3. Perhaps more interestingly, new occupied states, whose position is indicated by the dashed line near −6.5 eV, appear in the interface environment. These new interface states show contributions from mixed Ni *s* and *d* states and O *p* states in the Ni–O bond and Ni states of primarily *s* character, with states of mixed *s* and *p* character on the Si, for the Ni–Si bonds, indicating localized Ni–O and Ni–Si bonding of covalent nature. Naturally, this feature is not present in any of the isolated surface local DOS projections.

F4 Figure 4 displays the local DOS for the atoms involved in Ni–O and Ni–Al interactions (corresponding to the Ni, O, and Al of the Al_2O_3 row in Table II) at the Al_2O_3/Ni interface and in those corresponding cleaved surfaces. In contrast to the significant modification of the local DOS in the SiO_2/Ni interface, these plots for the Al_2O_3/Ni interface display less dramatic modifications. No additional new states appear on interface formation, unlike the case of SiO_2/Ni. The primary change to the local DOS in this interface structure is a shift to lower energy of the O and Al states in the interface environment. This is due to nickel screening of the Madelung potential imposed by the ceramic film and does not indicate local bonding interactions. These local DOS offer further confirmation to conclusions drawn from Table II, where Al_2O_3/Ni was anticipated to exhibit the weakest Ni–O bonding interactions.

The increased Ni–O bonding in SiO_2/Ni, relative to Al_2O_3/Ni, is likely to provide a major contribution to the three-times-larger adhesion calculated for the SiO_2(0001)/Ni(111) interface, relative to Al_2O_3(0001)/Ni(111). In TBC applications, one mechanism that leads to spallation of the ceramic coating is void formation at the interface of the metal alloy bond coat with the TGO. Of course, macroscopic mechanical contributions—strain due to thermal expansion mismatch, etc.—contribute to the failure of this interface. Additionally, our calculations suggest that intrinsic atomic-level weakness of the Al_2O_3/Ni interface, due to unfavorable local (closed-shell, repulsive) bonding interactions, may permit facile debonding and void formation at this site.[53,76] The Al_2O_3/Ni interface is a first-order approximation to typical TGO/NiCrAlY interfaces; hence, similar atomic-level void formation mechanisms may enhance failure at this site in TBCs. Increased local bonding at the SiO_2/Ni interface might inhibit such void formation and provide a preferable layer for oxidative protection, at least from a microscopic standpoint. Phase transitions and diffusion mechanisms are also crucial aspects of the macroscopic behavior of the coating. Based on our calculations, we suggest forms of silica-based TGO coatings could improve the lifetime of TBC operation by inhibiting oxide growth, void formation, and subsequent spallation. Such applications are also likely to require favorable ZrO_2–SiO_2 interactions; otherwise, the preferred failure site would merely be translated to an outer interface of the TBC. Accordingly, we investigate this ceramic/ceramic interface in the next section.

(3) ZrO_2(111)/SiO_2(0001) Interface

Achieving a small misfit when matching the surfaces of α-quartz(0001) with ZrO_2(111) requires a fairly large unique interface area (83.62 Å^2). The periodic cell for a 3-ML ZrO_2(111) coating on SiO_2(0001) is shown in Fig. 5. The interface matching F5 chosen for the *c*-ZrO_2(111)/α-SiO_2(0001) interface imposes a mismatch of only 1.9%. Maintaining a low misfit is crucial, because energy-dissipating mechanisms such as slip planes are not permitted by the periodic boundary conditions imposed with the calculation supercell. Similar to the surface terminations studied in the ZrO_2(001)/α-Al_2O_3($1\bar{1}02$) interface study of Christensen and Carter,[77] the SiO_2 and ZrO_2 surfaces are both oxygen-terminated to create stoichiometric, nonpolar surfaces. Such surfaces should result in a lower bound estimate for interface adhesion and reactivity: there is no strong chemical potential or polarity driving force to promote adhesion and/or new phase formation at the interface, and O–O bonding is not expected.

We find that the adhesion energy at this *c*-ZrO_2(111)/α-SiO_2(0001) interface is quite high: ~2.8 J/m^2 for the thickest ZrO_2 film studied (3 ML, ~7.5 Å thick). This value is more than a factor of 2 larger than the calculated adhesion at the ZrO_2/Al_2O_3 interface with a ZrO_2 film of similar thickness! Likewise, it is larger than the surface energies of either the SiO_2(0001) or ZrO_2(111) films. Local interfacial bonding interactions account for this dramatic increase in adhesion at the interface of ZrO_2 with SiO_2, relative to that with Al_2O_3. As we shall see, the ZrO_2/SiO_2 interface exhibits dramatic rearrangement of the atomic coordinates at the interface; in particular, the local electronic structure of the interfacial oxygens is modified significantly. The fairly strong

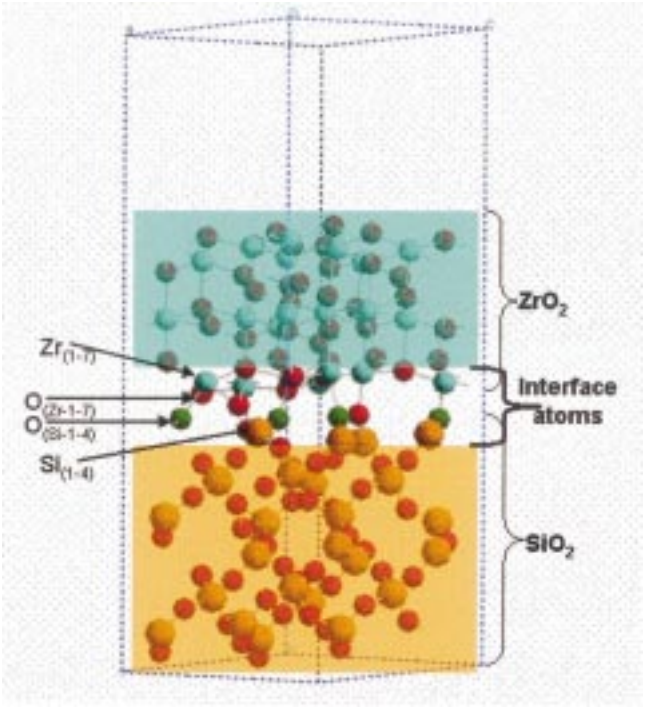

Fig. 5. Periodic cell of the 3-ML ZrO_2(111) coating on SiO_2(0001). In the SiO_2 region the Si atoms are represented by light-orange, larger spheres, and the O atoms are indicated by dark-orange, smaller spheres. In the ZrO_2 region, the Zr atoms are shown as light-blue stick-spheres, and the O atoms are indicated by red spheres. Substrate and coating slabs away from the interface are shaded, and the periodically unique atomic coordinates at the interface are indicated as "Interface atoms." Local details of interface bonding are presented in Table III. Interface atoms referenced to in Table III include (i) $Si_{(1)}$–$Si_{(4)}$, the orange spheres in the interface region; (ii) $Zr_{(1)}$–$Zr_{(7)}$, the blue spheres in the interface region; and (iii) $O_{(Si-1)}$–$O_{(Si-4)}$, the green spheres, and $O_{(Zr-1)}$–$O_{(Zr-7)}$, the red spheres in the interface region, corresponding to O atoms that were originally associated with the SiO_2 and ZrO_2 slabs, respectively.

covalent nature of the Si–O bond provides an explanation for this, with the local electronic structure of O in bulk SiO_2 being better approximated by O^- than O^{2-}, hence permitting additional bonding with increased coordination. As mentioned earlier, because of the complexity of the interface supercell, the interface structures we have found likely represent local minima on the potential-energy surface. However, finding more stable minima would only serve to increase the interface adhesion energy; hence, the comparisons to ZrO_2/Al_2O_3 and the results discussed here apply as general features to the ideal *c*-ZrO_2(111)/α-SiO_2(0001) interface.

In contrast to the SiO_2/Ni interface, the ZrO_2/SiO_2 interface displays significant relaxation effects both at the interface and within the ZrO_2 film. These relaxations correspond to two types. The first is a partial phase transition to the more stable *m*-ZrO_2 structure. This is most pronounced in thicker ZrO_2 films (≥3 ML), because the thinner films cannot effectively model bulklike behavior in the film interior. This phase transition is to be expected for the following reasons: (i) the monoclinic phase is the most stable polymorph of ZrO_2 at low temperature and ambient pressure, and (ii) the molar volume of the monoclinic phase is 4% larger than that of the tetragonal/cubic phases, and the ZrO_2 in-plane lattice vectors are expanded slightly to create a commensurate supercell from the initial 1.9% mismatch. The first explanation is likely to be the most important, considering that a similar monoclinic transformation was observed in ZrO_2/Al_2O_3 calculations where the ZrO_2 lattice was initially compressed for lock-in with the alumina substrate.[77] Moreover, in ZrO_2 film deposition experiments on a sapphire substrate, a partial transition from cubic to monoclinic is observed beyond a critical film thickness for slow deposition, and pure monoclinic phase results with faster deposition rates at elevated temperatures.[78] Therefore, independent of slight compression or expansion, the pure *c*-ZrO_2 films transform to the monoclinic structure. In addition to the phase transition, the second relaxation is a dramatic rearrangement induced by interfacial bonding. The interfacial O atoms rearrange such that the Si atoms nearest the interface tend to regain their crystalline fourfold oxygen coordination. These interface relaxations also promote increased O coordination with the interfacial Zr. As mentioned earlier, increased O coordination around both cations at the interface provides some explanation of the predicted large adhesive strength of this interface.

Table III, similar to Table I for SiO_2/Ni, provides a more quantitative picture of the local bonding interactions at the ZrO_2(111)/SiO_2(0001) interface. This table displays the site-projected charge difference between the interface and isolated surface environments. The charge perturbation due to formation of the ZrO_2/SiO_2 interface appears very dramatic, as evidenced by large site-projected charge differences of up to 0.63 e. This table also displays the identity of the atom to which the interface bond is formed and the corresponding bond lengths. The atoms are labeled according to the unique atomic sites on either side of the interface; i.e., $Si_{(4)}$ corresponds to the fourth unique silicon interfacial site, $O_{(Si-1)}$ corresponds to the first of four unique O sites associated with the SiO_2 side of the interface, $O_{(Zr-1)}$ corresponds to the first of seven unique interfacial O sites associated with the ZrO_2 side of the interface, etc. (see Fig. 5). On the SiO_2 side of the interface, all Si and O interfacial sites form favorable bonds, except in the case of $Si_{(2)}$, where the nearest interfacial atom is a distant (3.33 Å) Zr atom. This $Si_{(2)}$ is also the only atomic site on the SiO_2 side of the interface that does not gain projected charge in the interfacial environment. The more open

Table III. Site-Projected Charge Differences between Atoms at the SiO_2/ZrO_2 Interface and Those Atoms in the "Instantaneously" Cleaned Surfaces[†]

Site	Charge (e)	Bonded to	Bond length (Å)
	SiO_2 side		
$Si_{(1)}$	0.17	$O_{(Zr-3)}$	1.64
$O_{(Si-1)}$	0.36	$Zr_{(3)}$	2.05
$Si_{(2)}$	−0.03	($Zr_{(4)}$)	(3.33)
$O_{(Si-2)}$	0.20	$Zr_{(4)}$	2.13
$Si_{(3)}$	0.21	$O_{(Zr-6)}$	1.59
$O_{(Si-3)}$	0.33	$Zr_{(1)}$	2.12
$Si_{(4)}$	0.19	$O_{(Zr-7)}$	1.61
$O_{(Si-4)}$	0.36	$Zr_{(7)}$	2.02
	ZrO_2 side		
$Zr_{(1)}$	0.01	$O_{(Si-3)}$	2.12
$O_{(Zr-1)}$	0.26		
$Zr_{(2)}$	−0.15	($Si_{(2)}$)	(3.33)
$O_{(Zr-2)}$	0.25		
$Zr_{(3)}$	0.05	$O_{(Si-1)}$	2.05
$O_{(Zr-3)}$	0.56	$Si_{(1)}$	1.64
$Zr_{(4)}$	0.05	$O_{(Si-2)}$	2.13
$O_{(Zr-4)}$	0.38		
$Zr_{(5)}$	−0.01		
$O_{(Zr-5)}$	0.35		
$Zr_{(6)}$	−0.10	($Si_{(3)}$)	(3.47)
$O_{(Zr-6)}$	0.63	$Si_{(3)}$	1.59
$Zr_{(7)}$	0.10	$O_{(Si-4)}$	2.02
$O_{(Zr-7)}$	0.59	$Si_{(4)}$	1.61

[†]Bond lengths and interfacial atoms involved in those bonds are also indicated. Atoms are labeled according to the unique atomic sites on either side of the interface, i.e., $Si_{(4)}$ corresponds to the fourth unique silicon interfacial site, $O_{(Si-1)}$ corresponds to the first of four unique oxygen sites associated with the silica side of the interface, $O_{(Zr-1)}$ corresponds to the first of seven unique interfacial oxygen sites associated with the zirconia side of the interface, etc. Cases with bond lengths in parentheses merely indicate the nearest neighbor across the interface, where the long length suggests a conventional "bond" is not formed with this "coordination."

structure of the SiO_2 does not allow for complete interfacial bonding for all atoms from the ZrO_2 side of the interface. This can be seen in that $O_{(Zr-1)}$, $O_{(Zr-2)}$, $O_{(Zr-4)}$, and $O_{(Zr-5)}$, as well as $Zr_{(5)}$ (and effectively $Zr_{(6)}$), do not gain coordination from the SiO_2 surface in the relaxed interface structure. Nevertheless, even the O sites that do not experience any increased coordination display significant charge gain (0.25–0.38 e) in the interface, relative to the surface. The O sites that do experience increased coordination, by forming bonds with Si at the interface, experience an even larger (0.56–0.63 e) increase in local charge as a result, consistent with the electropositive nature of silicon. This occurs somewhat at the expense of the Zr to which the O are bonded for $Zr_{(2)}$ and $Zr_{(6)}$ positions, which are bonded to $O_{(Zr-7)}$ and $O_{(Zr-6)}$, respectively.

T4 Table IV shows the lengths of the interface bonds formed at the ZrO_2/Al_2O_3 and the ZrO_2/SiO_2 interfaces and the bulk crystal equilibrium bond lengths of several corresponding oxides. In both ceramic/ceramic interfaces, bond lengths near the optimum values for bulk α-quartz, α-Al_2O_3, and *t*- or *m*-ZrO_2 are formed across the interface. Bond lengths alone cannot explain the more than twofold increase in adhesion of the ZrO_2/SiO_2 interface, relative to ZrO_2/Al_2O_3. The charge difference evaluated in the ZrO_2/Al_2O_3 study was very small, with maximum differences of −0.05 e on the interfacial Zr and 0.06 e on the zirconia O.[77] We cannot compare these charge differences directly with those we computed for the ZrO_2/SiO_2 interface, because the integration spheres were chosen in a very different manner. Qualitatively, the values of Table III indicate that the charge redistribution at the ZrO_2/SiO_2 interface is significantly greater, with some sites experiencing differences that are a factor of 10 larger than those reported for the ZrO_2/Al_2O_3 interface!

F6 Figure 6, similar to Fig. 2 for the SiO_2/Ni interface, displays cross sections of charge-density differences between the interface and the sum of the (frozen) isolated surfaces for several cuts of interest. Figure 6(a) displays a cut near a typical Zr–O interface bond ($Zr_{(3)}$–$O_{(Si-1)}$ from Table III), Fig. 6(b) shows such a cut for a Si–O bond ($Si_{(4)}$–$O_{(Zr-7)}$ in Table III), and Fig. 6(c) displays the density difference near the $Si_{(2)}$–$O_{(Si-2)}$–$Zr_{(4)}$ bond from Table III. This last panel displays an instance where a Zr–O bond is created across the interface, whereas the Si bonded to that O does not experience an increased coordination. The contours represent similar (6.7×10^{-2} e/Å^3) density differences as those in Fig. 2. This ceramic/ceramic interface experiences much more dramatic density perturbations on interface formation than those exhibited by the metal/ceramic. These strong features are not very surprising when one compares the magnitudes of projected charge differences in Table I to those in Table III. The plots shown in Fig. 6 indicate that strongly polar–covalent bonds, i.e., density buildup between the nuclei but primarily associated with the oxygen, are formed in each instance. A more quantitative interpretation must include local DOS analysis.

Before investigating the local DOS projected onto the atomic sites in the interfacial environment, it is useful to compare such
F7 spectra from the bulk crystals. Figure 7 displays the local DOS projected onto representative cation and anion sites in bulk α-quartz and c-ZrO_2. The vertical axis shows the DOS. In each case, the zero of energy has been set to the Fermi level. Both crystals display valence band states in the region spanning −3.3 eV to 0.0 eV. Whereas the ZrO_2 local DOS also show valence states in the region of −5.6 eV to −3.3 eV, the SiO_2 spectra display an absence of states in the region of −4.6 eV to −3.3 eV. ZrO_2 exhibits a large gap from the top of the O 2*s* band (−15.5 eV) to the bottom of the valence band (−5.6 eV), whereas the SiO_2 spectra display Si–O bonding states in the region of −9.5 to −4.6 eV. The greatest number of states in this Si–O bonding region is available near −5.5 eV, close to the region of the lowest energy states in the valence band of ZrO_2. The top of the band that is composed primarily of O 2*s* states (−17.0 eV) is somewhat lower in energy in SiO_2 than in the ZrO_2 spectra. These local DOS plots display significant mixing of the O 2*p* states with the valence Si and Zr states for SiO_2 and ZrO_2, respectively.

F8 Figure 8 displays the local DOS on Si and O atoms near the ZrO_2/SiO_2 interface and those corresponding projections in the instantaneously cleaved SiO_2 surface. For ease of viewing, the vertical axis in Figs. 8(c) and (d) spans half the range (scale is expanded by a factor of 2) of that shown for Figs. 7, 8(a), and 8(b). These plots exhibit several interesting features. Overall, the interface stabilizes these states, as indicated by the downward shift of most energy levels. The bonding states near −5.5 eV, similar to those found in bulk SiO_2, appear most pronounced in Figs. 8(b) and (d). These atomic sites correspond to the Si–O bond where the Si does not gain coordination at the interface ($Si_{(2)}$–$O_{(Si-2)}$). Although Table III shows that this $Si_{(2)}$ loses some charge in the interface environment, its total integrated charge remains higher (by 0.14–0.18 e) than the other interfacial Si sites that gain coordination and charge in the interface environment, and the Si–O bond is very short at only 1.48 Å. Interestingly, both local DOS plots for O (Figs. 8(a) and (b)) do not show significant states in the region below −5.5 eV; hence, these local DOS on these O atoms resemble the local DOS plots for oxygen in ZrO_2 more than those for bulk SiO_2. Each O gains electronic charge (0.2–0.4 e) in the interface environment, as shown in Table III, which suggests increased polar covalent and/or ionic character to the bonding at the interface.

F9 Figure 9, similar to Fig. 8, shows the local DOS on Zr and O atoms near the ZrO_2/SiO_2 interface and those corresponding projections in the instantaneously cleaved surface. Also similar to Fig. 8, the vertical axis in Figs. 9(c)–(e) is magnified by a factor of 2, for ease of viewing. Strikingly, in this case, there is an overall destabilization (upward shift) of most energy levels upon formation of the interface. However, the interface local DOS plots resemble those on the Zr and O sites in bulk ZrO_2, i.e., the occupied valence states are primarily in the −5.5 to ~0.0 eV region. Although the features of the individual O and Zr plots in the surface environment differ from each other, the increased local coordination with the presence of the SiO_2 results in the interface local DOS plots appearing fairly similar for the two O and three Zr plots, respectively. Perhaps the main exceptions to this are the states near −5.5 eV in the plots shown in Figs. 9(a) and (c). In the case of Fig. 9(c), this coincides with the similar states on the SiO_2 side of the interface (Figs. 8(b) and (d)), because that Zr is coordinated with the O shown in Fig. 8(b). Figure 9(a) displays the local DOS projected onto an O that is bonded to a Zr ($Zr_{(5)}$ in Table III) that does not gain oxygen coordination at the interface. Most oxygen local DOS plots at the interface assume features that are similar to bulk ZrO_2 rather than bulk SiO_2, whereas the Zr and Si local DOS plots are fairly similar to those found in the respective bulk crystals.

The interfacial O from both the ZrO_2 and SiO_2 sides of the interface display valence bands that are similar to those found in bulk ZrO_2. Upon interface formation, both the Si and Zr gain O coordination at the interface to achieve bonds to oxygen that are comparable in length to those found in their respective bulk crystals (Table III). The heat of formation per mole of oxygen of ZrO_2 (550.3 kJ/(mol O)) is larger than that of SiO_2 (455.4 kJ/(mol O)).[79] It is also likely that the "amorphous" structure of the interface tends to favor bonding with less rigid bond-angle requirements, i.e., the more ionic ZrO_2-type bonding. Accordingly, although the interfacial O atoms equally coordinate with both

Table IV. Lengths of Interfacial Bonds Formed at the ZrO_2/Al_2O_3 and ZrO_2/SiO_2 Interfaces, and Bulk Crystal Equilibrium Bond Lengths of Several Corresponding Oxides

Material(s)	Bond length (Å)		
	X–O	Zr–O	X–Zr
ZrO_2/SiO_2	1.59–1.64	2.02–2.13	3.33–3.47
ZrO_2/Al_2O_3	1.91	2.09	2.98, 3.05
α-Al_2O_3	1.87		
α-SiO_2	1.61		
ZrO_2[†]		~2.22 (*c*), ~2.06 (*m*), ~2.10 (*t*)	

[†]Letters in parentheses (*c*, *m*, and *t*) denote cubic, monoclinic, and tetragonal, respectively.

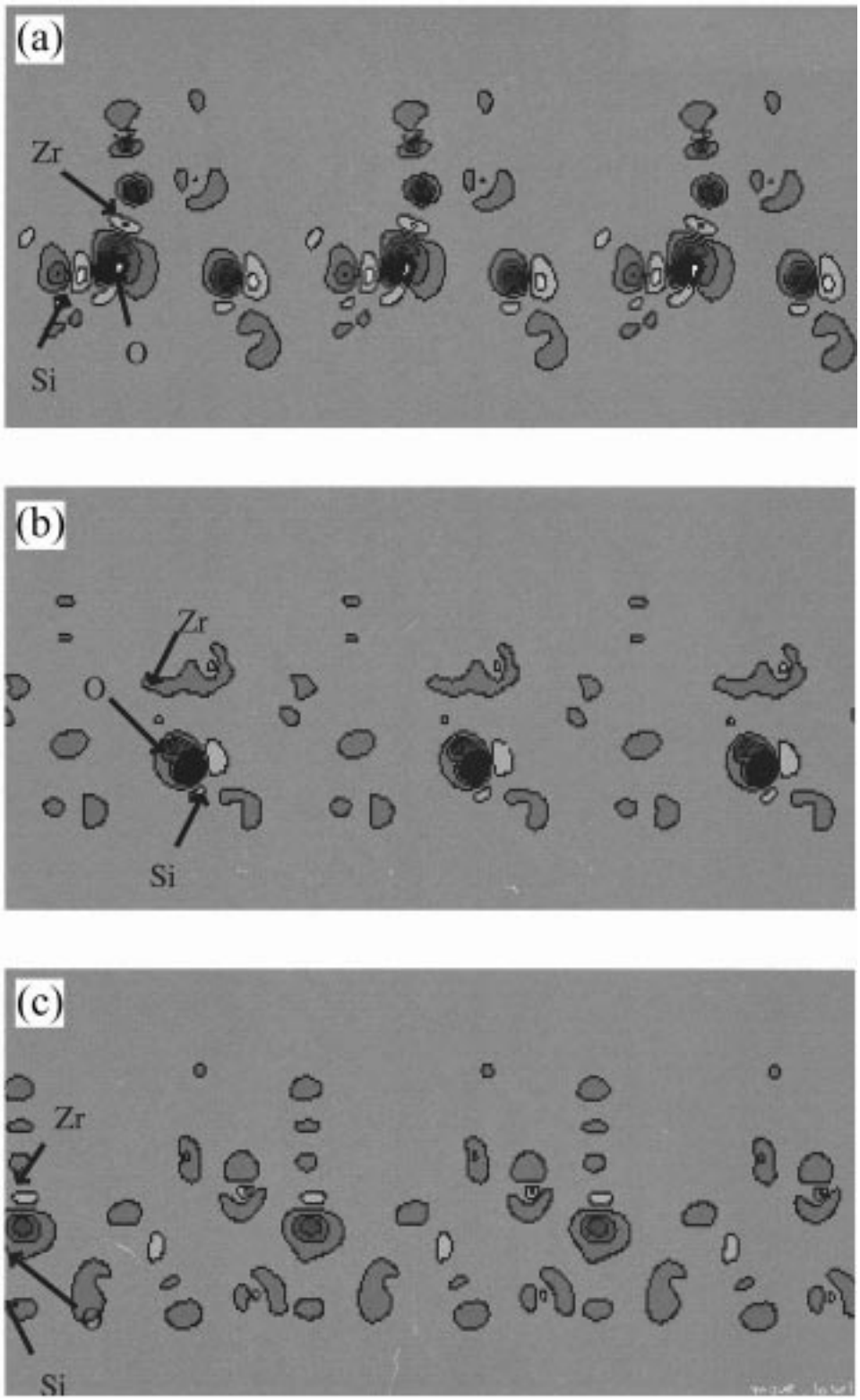

Fig. 6. Electron density difference plots for 2D slices perpendicular to the ZrO_2/SiO_2 interface for (a) a Zr–O bond, (b) a Si–O bond, and (c) a Zr–O bond formed with no increased O coordination on the Si. Same gray scale used in all plots.

types of cations, the resulting electronic structure indicates the interfacial O atoms are reduced in the interface environment and become more ZrO_2-like.

IV. Conclusions

In previous studies, we investigated the ideal interfaces formed between Al_2O_3/Ni[53] and ZrO_2/Al_2O_3.[77] Both interfaces exhibited weak adhesion; this was especially dramatic in the case of thicker Al_2O_3 films on the metal substrate. We postulated that an inherent atomic-level weakness of such interfaces was due to closed-shell repulsions. For Al_2O_3/Ni, these arise from the O anions and the nearly filled *d* shell of the Ni; in the case of ZrO_2/Al_2O_3, the significant ionic character to the bonding in both oxides results in effectively closed-shell O anions. To minimize such effects at these interfaces, we investigated the effect of doping the Al_2O_3/Ni

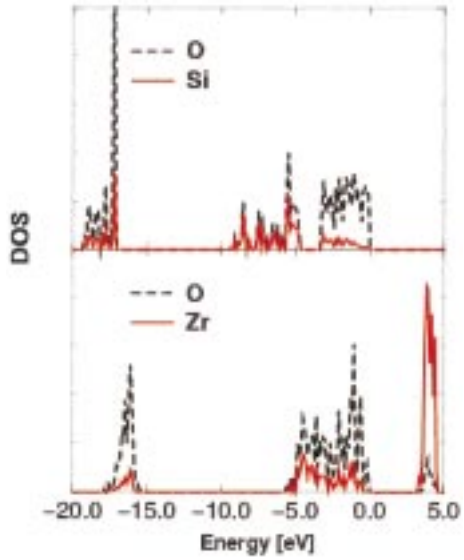

Fig. 7. Local DOS projected onto representative atomic sites of the bulk α-SiO_2 and cubic ZrO_2 crystals. The zero of energy has been set to the Fermi level.

interface with early transition metals, which have open *d* shells.[61,76,80] These modifications to the local electronic structure of the interface dramatically increased interface adhesion. We also speculated that closed-shell repulsions at heterogeneous interfaces might be alleviated with modification of the O anion electronic structure in the oxide.[61,80] To this end, we have investigated the interfaces of nickel and ZrO_2 with a more covalently bonded oxide, SiO_2.

We presented the detailed interactions that occur at an interface between the late transition metal (nickel) and a ceramic with significant covalent character in its bonding (SiO_2). The significantly increased interface adhesion of the SiO_2/Ni interface, compared with the Al_2O_3/Ni interface (three times stronger!), appears to arise from local bonding of predominantly polar covalent character. In particular, the Ni–O interactions, which appear repulsive in Al_2O_3/Ni,[76,80] are more favorable with SiO_2.

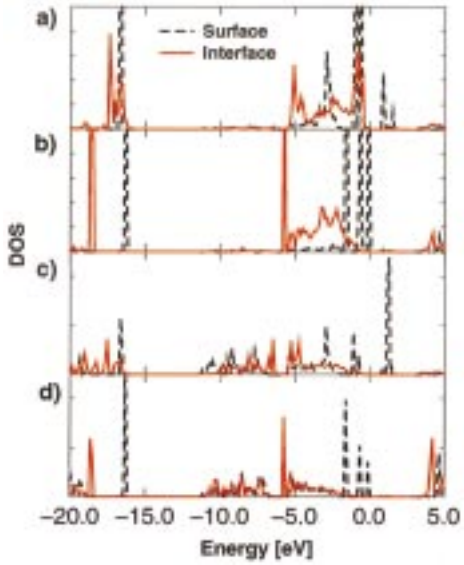

Fig. 8. Local DOS projected onto several unique atomic sites in the ZrO_2/SiO_2 interface and the isolated SiO_2 surface immediately after cleaving, i.e., the positions of the surface atoms are identical to those of the interface ((a) $O_{(Si\text{-}4)}$, (b) $O_{(Si\text{-}2)}$, (c) $Si_{(3)}$, and (d) $Si_{(2)}$ from Table III).

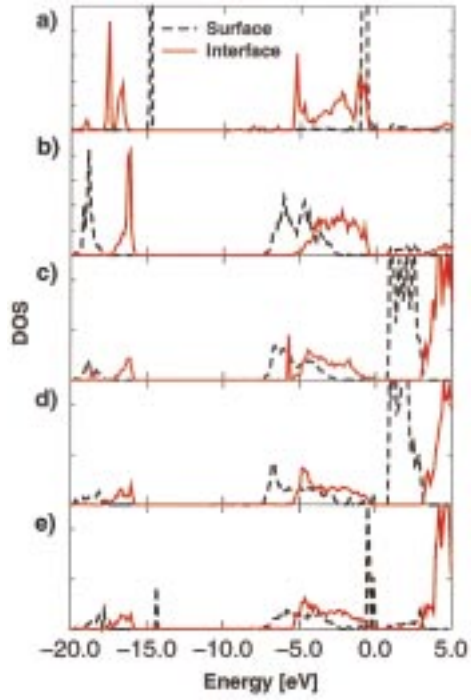

Fig. 9. Local DOS projected onto several unique atomic sites in the ZrO_2/SiO_2 interface and the isolated ZrO_2 surface immediately after cleaving, i.e., the atomic positions of the surface atoms are identical to those of the interface ((a) $O_{(Zr\text{-}6)}$, (b) $O_{(Zr\text{-}1)}$, (c) $Zr_{(4)}$, (d) $Zr_{(3)}$, and (e) $Zr_{(2)}$ from Table III).

The more covalent nature of SiO_2 results in reduced repulsions between the Ni 3*d* shell and the O atoms in SiO_2 (relative to more ionic oxides), as well as more covalent Ni–O bonding. We speculate that the increased local bonding and adhesion for the SiO_2 coating should inhibit void formation at this interface, relative to those formed with more ionic oxides that exhibit repulsive Ni–O interactions.

Our investigation of the ZrO_2/SiO_2 interface shows stronger bonding than that exhibited by the interface of zirconia with the more ionic Al_2O_3 substrate. The stoichiometric ZrO_2 does not reduce the SiO_2, as might be expected for a ZrO_{2-x} oxide; however, the interfacial O ions that are associated with both the SiO_2 and ZrO_2 sides of the interface do exhibit electronic structures that are more similar to bulk O ions in ZrO_2. Increased ionic character to the interfacial O-cation bonding permits less rigid geometric requirements for these interfacial bonds, which minimizes strain at the interface. The "amorphous" bonding (in that the Si–O and Zr–O bond lengths are not uniform) across the interface serves to increase local coordination of both Si and Zr, thus resulting in a large ZrO_2/SiO_2 ideal work of adhesion. We find very strong bonding at this interface, as might have been anticipated from SEM and TEM studies of ZrO_2 films on glass ceramics[37] and the slight negative enthalpy for SiO_2 reacting with ZrO_2.[44]

At elevated temperatures, it can be expected that both the SiO_2/Ni and the ZrO_2/SiO_2 interfaces will be somewhat reactive. The heats of formation per mole of O indicate that the most stable oxide of Ni is over 200 kJ less stable than SiO_2,[81] while SiO_2 is only ~50 kJ less stable than ZrO_2 per mole of O.[79] Our results for the interface of nickel with SiO_2, as well as with Al_2O_3 and ZrO_2, suggest that chemical bonding provides a significant source of interface strengthening, even at 0 K and in the absence of a new reaction phase. Nonreactive interfaces can form weak, strained bonds with minimal internal bonding strains within the ceramic and/or metal; in the case of stronger interface interactions, interface bonding may be sufficiently favorable even to allow for slight straining of the intraceramic or intrametal bonding, as seen at the SiO_2/Ni interface.

Although many TBC performance goals have been understood for decades, optimizing the performance of these coatings for particular applications remains an active area of research. As mentioned earlier, silica coatings have shown very favorable oxidation/corrosion protection on certain alloys, and mullite coatings display promise in protecting silicon carbide and silicon nitride ceramics. To our knowledge, silica or mullite coatings have not been well-studied for nickel-based superalloy applications with YSZ thermal protective coatings. Of course, temperature effects are likely to play an important role, and SiO_2 phase changes under extreme thermal cycling may limit practical applications of such a protective oxide. However, in TBC applications, the YSZ top coat will provide some thermal protection to both the underlying oxides and the metal alloy substrate, hence limiting the extreme temperatures to which the SiO_2 might be exposed. The favorable local adhesion at these interfaces suggests such coatings might exhibit improved resistance to debonding, void formation, and subsequent spallation under thermal cycling conditions.

Acknowledgment

The authors thank Prof. Rick Garfunkel for helpful discussions regarding the suitability of SiO_2 as a low-oxygen-mobility oxide.

References

[1]A. Christensen, E. A. A. Jarvis, and E. A. Carter, "Atomic-Level Properties of Thermal Barrier Coatings: Characterization of Metal–Ceramic Interfaces"; pp. 490–546 in Advanced Series in Physical Chemistry, Vol. 11, *Chemical Dynamics in Extreme Environments*. Edited by R. Dressler. World Scientific, Princeton, NJ, 2001.

[2]N. P. Padture, M. Gell, and E. H. Jordan, "Thermal Barrier Coatings for Gas-Turbine Airfoils," *Science*, **296**, 280–84 (2002).

[3](a)P. Hancock and J. R. Nicholls, *Coatings for Heat Engines*; pp. 31–58. Edited by R. L. Clarke. Department of Energy, Washington, DC, 1984. (b)J. R. Nicholls and P. Hancock, "Advanced High Temperature Coatings for Gas Turbines," *Ind. Corros.*, **5** [4] 8–18 1987.

[4]G. W. Goward, "Progress in Coatings for Gas Turbine Airfoils," *Surf. Coat. Technol.*, **108–109** [1–3] 73–79 (1998).

[5]J. A. Haynes, M. K. Ferber, W. D. Porter, and E. D. Rigney, "Characterization of Alumina Scales Formed during Isothermal and Cyclic Oxidation of Plasma-Sprayed TBC Systems at 1150°C," *Oxid. Met.*, **52** [1–2] 31–76 (1999).

[6]D. P. Whittle and J. Stringer, "Improvements in High Temperature Oxidation Resistance by Additions of Reactive Elements or Oxide Dispersions," *Philos. Trans. R. Soc. London A*, **295** [1413] 309–29 (1980).

[7]F. H. Stott, G. C. Wood, and J. Stringer, "The Influence of Alloying Elements on the Development and Maintenance of Protective Scales," *Oxid. Met.*, **44** [1–2] 113–45 (1995).

[8]F. H. Stott, "Methods of Improving Adherence," *Mater. Sci. Technol.*, **4** [5] 431–38 (1988).

[9]B. A. Pint, I. G. Wright, W. Y. Lee, Y. Zhang, K. Prussner, and K. B. Alexander, "Substrate and Bond Coat Compositions: Factors Affecting Alumina Scale Adhesion," *Mater. Sci. Eng. A*, **245** [2] 201–11 (1998).

[10]Y. F. Han, Z. P. Xing, M. C. Chaturvedi, and Q. Xu, "Oxidation Resistance and Microstructure of Ni-Cr-Al-Y-Si Coating on Ni_3Al Based Alloy," *Mater. Sci. Eng. A.*, **239–240**, 871–76 (1997).

[11]S. R. J. Saunders and J. R. Nicholls, "Coatings and Surface Treatments for High Temperature Oxidation Resistance," *Mater. Sci. Technol.*, **5** [8] 780–98 (1989).

[12]N. S. Jacobson, E. J. Opila, D. S. Fox, and J. L. Smialek, "Oxidation and Corrosion of Silicon-Based Ceramics and Composites," *Mater. Sci. Forum*, **251–254** [2] 817–32 (1997).

[13]A. Kumar and D. L. Douglass, "Modification of the Oxidation Behavior of High-Purity Austenitic Fe-14Cr-14Ni by the Addition of Silicon," *Oxid. Met.*, **10** [1] 1–22 (1976).

[14]H. E. Evans, D. A. Hilton, R. A. Holm, and S. J. Webster, "The Development of Localized Pits during Stainless Steel Oxidation," *Oxid. Met.*, **14** [3] 235–47 (1980).

[15]H. E. Evans, D. A. Hilton, R. A. Holm, and S. J. Webster, "Influence of Silicon Additions on the Oxidation Resistance of a Stainless Steel," *Oxid. Met.*, **19** [1–2] 1–18 (1983).

[16]D. G. Lees, "On the Reasons for the Effects of Dispersions of Stable Oxides and Additions of Reactive Elements on the Adhesion and Growth-Mechanisms of Chromia and Alumina Scales—The 'Sulfur Effect'," *Oxid. Met.*, **27** [1–2] 75–81 (1987).

[17]F. C. J. Fellowes, W. M. Steen, and S. R. J. Saunders, "Deposition of Silica Coatings on Incoloy 800H Substrates Using a High Power Laser," *Surf. Coat. Technol.*, **45**, 425–34 (1991).

[18]R. Hofman, J. G. F. Westheim, T. Fransen, and P. J. Gellings, "The Protection of Alloys against High Temperature Sulphidation by SiO_2-Coatings Deposited by MOCVD," *Mater. Manuf. Processes*, **7** [2] 227–38 (1992).

[19]S. Ono, Y. Nishi, and S. Hirano, "Chromium-Free Corrosion Resistance of Metals by Ceramic Coating," *J. Am. Ceram. Soc.*, **84** [12] 3054–56 (2001).

[20]K. Bouhanek, D. Oquab, and B. Pieraggi, "High Temperature Oxidation of Single-Crystal Ni-Base Superalloys," *Mater. Sci. Forum*, **251–254** [1] 33–40 (1997).

[21]B. C. Valek and J. M. Hampikian, "Silica Thin Films Applied to Ni-20Cr Alloy via Combustion Chemical Vapor Deposition," *Surf. Coat. Technol.*, **94–95** [1–3] 13–20 (1997).

[22]B. Ahmad and P. Fox, "STEM Analysis of the Transient Oxidation of a Ni-20Cr Alloy at High Temperature," *Oxid. Met.*, **52** [1–2] 113–38 (1999).

[23]Z. Rao, J. S. Williams, A. P. Pogany, D. K. Sood, and G. A. Collins, "Nickel Silicide Formation in Silicon Implanted Nickel," *J. Appl. Phys.*, **77** [8] 3782–90 (1995).

[24]I. Grimberg and B. Z. Weiss, "Crystallization and Growth of Ni-Si Alloy Thin Films on Inert and on Silicon Substrates," *J. Appl. Phys.*, **77** [8] 3791–98 (1995).

[25]N. Sukidi, C. C. Koch, and C. T. Liu, "The Oxidation of Ni_3Si-Base Alloys," *Mater. Sci. Eng. A*, **191** [1–2] 223–31 (1995).

[26]K. Fritscher, C. Leyens, and M. Peters, "Development of a Low-Expansion Bond Coating for Ni-Base Superalloys," *Mater. Sci. Eng. A*, **190**, 253–58 (1995).

[27]S. Ramesh, Y. Cohen, D. Aurbach, and A. Gedanken, "Atomic Force Microscopy Investigation of the Surface Topography and Adhesion of Nickel Nanoparticles to Submicrospherical Silica," *Chem. Phys. Lett.*, **287** [3–4] 461–67 (1998).

[28]Z. Shi and M. A. Player, "Preferred Orientations of Evaporated Ni Films on Mo and SiO_2 Substrates," *Vacuum*, **49** [4] 257–63 (1998).

[29]S. Ramesh, Yu. Koltypin, R. Prozorov, and A. Gedanken, "Sonochemical Deposition and Characterization of Nanophasic Nickel on Silica Microspheres," *Chem. Mater.*, **9**, 546 (1997).

[30]R. Sangiorgi, M. L. Muolo, D. Chatain, and N. Eustathopoulos, "Wettability and Work of Adhesion of Nonreactive Liquid Metals on Silica," *J. Am. Ceram. Soc.*, **71** [9] 742–48 (1988).

[31]N. Eustathopoulos and B. Drevet, "Determination of the Nature of Metal-Oxide Interfacial Interactions from Sessile Drop Data," *Mater. Sci. Eng. A*, **249** [1–2] 176–83 (1998).

[32](a)N. Lopez, F. Illas, and G. Pacchioni, "Ab initio Theory of Metal Deposition on SiO_2. I. Cu_n (n = 1–5) Clusters on Nonbridging Oxygen Defects," *J. Phys. Chem. B*, **103** [10] 1712–18 (1999). (b)G. Pacchioni, N. Lopez, and F. Illas, "Cu Atoms and Clusters on Regular and Defect Sites of the SiO_2 Surface. Electronic Structure and Properties from First Principles Calculations," *Faraday Discuss.*, **114**, 209–22 (1999).

[33]G. Profeta, A. Continenza, and A. J. Freeman, "Energetics and Bonding Properties of the Ni/β-SiC (001) Interface: An *ab Initio* Study," *Phys. Rev. B: Condens. Matter*, **64** [4] 045303/1—045303/7 (2001).

[34](a)T. Schroeder, M. Adelt, B. Richter, M. Naschitzki, M. Bäumer, and H.-J. Freund, "Epitaxial Growth of SiO_2 on Mo(112)," *Surf. Rev. Lett.*, **7** [1–2] 7–14 (2000). (b)T. Schroeder, M. Adelt, B. Rishter, M. Naschitzki, M. Bäumer, and H.-J. Freund, "Growth of Well-Ordered Silicon Dioxide Films on Mo(112)," *Microelectronics Reliability*, **40** [4–5] 841–44 (2000).

[35]X. Y. Virieux, J. Desmaison, J. C. Labbe, and A. Gabriel, "Reactivity between Two Liquid Nickel-Base Superalloys with SiO_2 Ceramics," *Key Eng. Mater.*, **132–136**, 1657–60 (1997).

[36]M. Copel, M. Gribelyuk, and E. Gusev, "Structure and Stability of Ultrathin Zirconium Oxide Layers on Si(001)," *Appl. Phys. Lett.*, **76** [4] 436–38 (2000).

[37]L. Zeng, E. D. Case, and M. A. Crimp, "The Interfacial Microstructure of Zirconia and MaCor™ Joined Using Spin-On Layers," *Mater. Sci. Eng. A*, **307** [1–2] 74–79 (2001).

[38]C. C. Appel and N. Bonanos, "Structural and Electrical Characterization of Silica-Containing Yttria-Stabilised Zirconia," *J. Eur. Ceram. Soc.*, **19** [6–7] 847–51 (1999).

[39]Y.-M. Sun, J. Lozano, H. Ho, H. J. Parks, S. Veldman, and J. M. White, "Interfacial Silicon Oxide Formation during Synthesis of ZrO_2 on Si(100)," *Appl. Surf. Sci.*, **161** [1–2] 115–22 (2000).

[40]B. W. Busch, W. H. Schulte, E. Garfunkel, T. Gustafsson, W. Qi, R. Nieh, and J. Lee, "Oxygen Exchange and Transport in Thin Zirconia Films on Si(100)," *Phys. Rev. B: Condens. Matter*, **62** [20] R13290–93 (2000).

[41]F. del Monte, W. Larsen, and J. D. Mackenzie, "Chemical Interactions Promoting the ZrO_2 Tetragonal Stabilization in ZrO_2–SiO_2 Binary Oxides," *J. Am. Ceram. Soc.*, **83** [6] 1506–12 (2000).

[42]C. R. Aita, M. D. Wiggins, R. Whig, C. M. Scanlan, and M. Gajdardziska-Josifovska, "Thermodynamics of Tetragonal Zirconia Formation in a Nanolaminate Film," *J. Appl. Phys.*, **79** [2] 1176–78 (1996).

[43]Y.-H. Koh, Y.-M. Kong, S. Kim, and H.-E. Kim, "Improved Low-Temperature Environmental Degradation of Yttria-Stabilized Tetragonal Zirconia Polycrystals by Surface Encapsulation," *J. Am. Ceram. Soc.*, **82** [6] 1456–58 (1999).

[44]M. Gutowski, J. E. Jaffe, C.-L. Liu, M. Stoker, R. I. Hegde, R. S. Rai, and P. J. Tobin, "Thermodynamic Stability of High-K Dielectric Metal Oxides ZrO_2 and HfO_2 in Contact with Si and SiO_2," *Appl. Phys. Lett.*, **80** [11] 1897–99 (2002).

[45]P. Heydt, C. Luo, and D. R. Clarke, "Crystallographic Texture and Thermal Conductivity of Zirconia Thermal Barrier Coatings Deposited on Different Substrates," *J. Am. Ceram. Soc.*, **84** [7] 1539–44 (2001).

[46]A. Nazeri and S. B. Qadri, "Alumina-Stabilized Zirconia Coatings for High-Temperature Protection of Turbine Blades," *Surf. Coat. Technol.*, **86–87**, 166–69 (1996).

[47]K. N. Lee and R. A. Miller, "Development and Environmental Durability of Mullite and Mullite/YSZ Dual Layer Coatings for SiC and Si_3N_4 Ceramics," *Surf. Coat. Technol.*, **86–87** [1–3] 142–48 (1996).

[48](a)P. Hohenberg and W. Kohn, "Inhomogeneous Electron Gas," *Phys. Rev. B*, **136** [3B] 864 (1964). (b)W. Kohn and L. J. Sham, "Self-Consistent Equations Including Exchange and Correlation Effects," *Phys. Rev.*, **140** [4A] 1133 (1965).

[49](a)G. Kresse and J. Hafner, "*Ab Initio* Molecular Dynamics for Liquid Metals," *Phys. Rev. B: Condens. Matter*, **47**, 558 (1993). (b) G. Kresse and J. Hafner, "*Ab Initio* Molecular Dynamics Simulation of the Liquid–Metal–Amorphous–Semiconductor Transition in Germanium," *Phys. Rev. B: Condens. Matter*, **49**, 14251 (1994). (c)G. Kresse and J. Furthmüller, "Efficiency of *ab Initio* Total Energy Calculations for Metals and Semiconductors Using a Plane-Wave Basis Set," *Comput. Mater. Sci.*, **6**, 15 (1996).

[50]D. Vanderbilt, "Soft Self-Consistent Pseudopotentials in a Generalized Eigenvalue Formalism," *Phys. Rev. B: Condens. Matter*, **41** [11] 7892–95 (1990).

[51]See, for instance, the following literature: J. P. Perdew, "Density-Functional Approximation for the Correlation Energy of the Inhomogeneous Electron Gas," *Phys. Rev. B*, **33**, 8822 (1986); *ibid.*, "Erratum: Density-Functional Approximation for the Correlation Energy of the Inhomogeneous Electron Gas," **34**, 7406 (1986); J. P. Perdew, "Electronic Structure of Solids"; p. 11 in *Proceedings of the 75th WE-Heraeus-Seminar and 21st Annual International Symposium on Electronic Structure of Solids*. Edited by P. Ziesche and H. Eschrig. Akademie Verlag, Berlin, Germany, 1991; J. P. Perdew, J. A. Chevary, S. H. Vosko, K. A. Kackson, M. R. Pederson, D. J. Singh, and C. Fiolhais, "Atoms, Molecules, Solids, and Surfaces: Applications of the Generalized Gradient Approximation for Exchange and Correlation," *Phys. Rev. B*, **46**, 6671 (1992).

[52]A. Christensen and E. A. Carter, "Adhesion of Ultrathin ZrO_2(111) Films on Ni(111) from First Principles," *J. Chem. Phys.*, **114** [13] 5816–31 (2001).

[53]E. A. A. Jarvis. A. Christensen, and E. A. Carter, "Weak Bonding of Alumina Coatings on Ni(111)," *Surf. Sci.*, **487** [1–3] 55–76 (2001).

[54]G. Kresse and J. Hafner, "Norm-Conserving and Ultrasoft Pseudopotentials for First-Row and Transition Elements," *J. Phys. Condens. Matter*, **6** [40] 8245–57 (1994).

[55]S. G. Louie, S. Froyen, and M. L. Cohen, "Non-linear Ionic Pseudopotentials in Spin-Density-Functional Calculations," *Phys. Rev. B*, **26** [4] 1738–42 (1982).

[56]H. J. Monkhorst and J. D. Pack, "Special Points for Brillouin-Zone Integrations," *Phys. Rev. B*, **13**, 5188–92 (1976).

[57]N. D. Mermin, "Thermal Properties of the Inhomogeneous Electron Gas," *Phys. Rev. A*, **137** [5A] 1441–43 (1965).

[58]M. Methfessel and A. T. Paxton, "High-Precision Sampling for Brillouin-Zone Integration in Metals," *Phys. Rev. B: Condens. Matter*, **40** [6] 3616–21 (1989).

[59]P. E. Blöchl, O. Jepsen, and O. K. Andersen, "Improved Tetrahedron Method for Brillouin-Zone Integrations," *Phys. Rev. B: Condens. Matter*, **49** [23] 16223–33 (1994).

[60](a)S. Nosè, "A Unified Formulation of the Constant Temperature Molecular Dynamics Methods," *J. Chem. Phys.*, **81** [1] 511–19 (1984). (b)S. Nosè, "Constant Temperature Molecular Dynamics Methods," *Prog. Theor. Phys. Suppl.*, **103**, 1–46 (1991).

[61]E. A. A. Jarvis and E. A. Carter, "An Atomic Perspective of a Doped Metal–Oxide Interface," *J. Phys. Chem. B*, **106**, 7995 (2002).

[62]F. D. Murnaghan, "The Compressibility of Media under Extreme Pressures," *Proc. Natl. Acad. Sci.*, **30**, 2344 (1944).

[63]V. Swamy, S. K. Saxena, B. Sundman, and J. Zhang, "A Thermodynamic Assessment of Silica Phase Diagram," *J. Geophys. Res.*, **99** [B6] 11787–94 (1994).

[64]R. J. Hemley, C. T. Prewitt, and K. J. Kingma, "High-Pressure Behavior of Silica"; pp. 41–81 in *Silica: Physical Behavior, Geochemistry, and Materials Applications*, Reviews in Mineralogy, Vol. 29. Edited by P. J. Heaney, C. T. Prewitt, and G. V. Gibbs. Mineralogical Society of America, Washington, DC, 1994.

[65]J. D. Jorgensen, "Compression Mechanisms in α-quartz Structures—SiO_2 and GeO_2," *J. Appl. Phys.*, **49** [11] 5473–78 (1978).

[66]A. Christensen and E. A. Carter, "First-Principles Study of the Surfaces of Zirconia," *Phys. Rev. B: Condens. Matter*, **58** [12] 8050–64 (1998).

[67]F. Bart, M. Gautier, F. Jollet, and J. P. Duraud, "(0001) Quartz Surface Imperfections," *J. Phys. IV*, **4** [C2] 195–98 (1994).

[68]F. Bart and M. Gautier, "A LEED Study of the (0001) α-quartz Surface Reconstruction," *Surf. Sci.*, **311** [1–2] L671–L676 (1994).

[69]See, for example: J. Q. Broughton, F. F. Abraham, N. Berstein, and E. Kaxiras, "Concurrent Coupling of Length Scales: Methodology and Application," *Phys. Rev. B: Condens. Matter*, **60**, 2391–403 (1999); M. Ortiz, A. M. Cuitiño, J. Knap, and M. Koslowski, "Mixed Atomistic-Continuum Models of Material Behavior: The Art of Transcending Atomistics and Informing Continua," *MRS Bull.*, **26** [3] 216–21 (2001).

[70]See, for example, the following literature: W. Kohn, "Density Functional and Density Matrix Method Scaling Linearly with the Number of Atoms," *Phys. Rev. Lett.*, **76**, 3168 (1996); P. Ordejón, "Order-N Tight-Binding Methods for Electronic Structure and Molecular Dynamics," *Comp. Mater. Sci.*, **12**, 157 (1998); R. Baer and M. Head-Gordon, "Energy Renormalization-Group Method for Electronic Structure of Large Systems," *Phys. Rev. B: Condens. Matter*, **58**, 15296 (1998).

[71]See, for example, the following literature: Y. A. Wang and E. A. Carter, "Orbital-Free Kinetic Energy Density Functional Theory"; pp.117–84 in Progress in Theoretical Chemistry and Physics Series, *Theoretical Methods in Condensed Phase Chemistry*. Edited by S. D. Schwartz. Kluwer, Amsterdam, The Netherlands, 2000; S. C. Watson and E. A. Carter, "Linear Scaling Parallel Algorithms for the First Principles Treatment of Metals," *Comput. Phys. Commun.*, **128**, 67 (2000); S. Goedecker, "Linear Scaling Electronic Structure Methods," *Rev. Mod. Phys.*, **71**, 1085 (1999).

[72]J. Goniakowski and C. Noguera, "Electronic Structure of Clean Insulating Oxide Surfaces I. A Numerical Approach," *Surf. Sci.*, **319** [1–2] 68–80 (1994).

[73](a)M. V. Koudriachova, J. V. L. Beckers, and S. W. de Leeuw, "Comparison of *ab Initio* and Empirical Approaches to the Quartz Surface," *Comp. Mater. Sci.*, **17**, 182–85 (2000). (b)M. V. Koudriachova, J. V. L. Beckers, and S. W. de Leeuw, "Computer Simulation of the Quartz Surface: A Combined *ab Initio* and Empirical Potential Approach," *Comp. Mater. Sci.*, **20** [3–4] 381–86 (2001).

[74]J. T. Klomp, "Ceramic–Metal Interactions," *Mater. Res. Soc. Symp. Proc.*, **40**, 381–91 (1985).

[75](a)W. Kohn, *Phys. Rev.*, **115**, 809 (1959). (b)S. Ismail-Beigi and T. A. Arias, *Phys. Rev. Lett.*, **82**, 2127 (1999). (c)E. A. A. Jarvis, R. L. Hayes, and E. A. Carter, "Effects of Oxidation on the Nanoscale Mechanisms of Crack Formation in Aluminum," *Chem. Phys. Chem.*, **2**, 55 (2001).

[76]E. A. A. Jarvis and E. A. Carter, "The Role of Reactive Elements in Thermal Barrier Coatings," *Comp. Sci. Eng.*, **4** [2] 33–41 (2002).

[77]A. Christensen and E. A. Carter, "First-Principles Characterization of a Hetero-ceramic Interface: ZrO_2(001) Deposited on an α-Al_2O_3(11$\bar{1}$02) Substrate," *Phys. Rev. B: Condens. Matter*, **62** [24] 16968–83 (2000).

[78]S. C. Moulzolf, Y. Yu, D. J. Frankel, and R. J. Lad, "Properties of ZrO_2 Films on Sapphire Prepared by Electron Cyclotron Resonance Oxygen-Plasma-Assisted Deposition," *J. Vac. Sci. Technol. A*, **15** [3] 1211–14 (1997).

[79]D. R. Lide (ed.), *CRC Handbook of Chemistry and Physics*; 80th Ed. CRC Press, Washington, DC, 1999.

[80]E. A. Jarvis and E. A. Carter, "Importance of Open-Shell Effects in Adhesion at Metal–Ceramic Interfaces," *Phys. Rev. B: Condens. Matter*, **66**, 100103 (2002)

[81]C. T. Campbell, "Ultrathin Metal Films and Particles on Oxide Surfaces: Structural, Electronic and Chemisorptive Properties," *Surf. Sci.*, **27** [1–3] 1–111 (1997). □

Emily A. Jarvis currently is sponsored by the American Chemical Society to serve as a Congressional Science Fellow in the U.S. Senate through the American Association for the Advancement of Science. Dr. Jarvis earned her doctorate while working in Professor Emily Carter's research group at UCLA. Her research employed density functional calculations to investigate atomic-level aspects of materials failure and to suggest chemical modifications designed to improve materials performance. In particular, this work focused on enhancing adhesion at metal/ceramic interfaces for high-temperature applications. Dr. Jarvis' research received several awards, including the Materials Research Society Gold Award and the UCLA Physical Chemistry Dissertation Award.

Emily Carter is a Professor of Chemistry and Materials Science at the University of California, Los Angeles, and is UCLA's Director of Modeling and Simulation for the California NanoSystems Institute. A theoretical physical chemist, she develops and applies computational methods from various fields: quantum chemistry, solid-state physics, and mechanical engineering in an effort to understand what chemical and mechanical effects cause materials to fail as well as how to optimally prevent them from failing. The author of more than 130 publications and more than 215 invited lectures, Dr. Carter's work has garnered her a number of national and international awards and fellowships.